Nano Energy 76 (2020) 105067

Contents lists available at ScienceDirect

Nano Energy

journal homepage: http://www.elsevier.com/locate/nanoen

A unified contact force-dependent model for triboelectric nanogenerators accounting for surface roughness

Yang Xu [a,b], Guanbo Min [a,b], Nikolaj Gadegaard [c], Ravinder Dahiya [b,*], Daniel M. Mulvihill [a,*]

[a] Materials and Manufacturing Research Group, James Watt School of Engineering, University of Glasgow, Glasgow, G12 8QQ, UK
[b] Bendable Electronics and Sensing Technologies (BEST) Group, James Watt School of Engineering, University of Glasgow, Glasgow, G12 8QQ, UK
[c] Division of Biomedical Engineering, James Watt School of Engineering, University of Glasgow, Glasgow, G12 8LT, UK

ARTICLE INFO

Keywords:
Triboelectric nanogenerator
Theory
Surface roughness
Contact area
Force-dependent electrical performance
Distance-dependent electric field

ABSTRACT

Triboelectric nanogenerators (TENGs) allow generation of electricity based on charge transfer during repeated contact of suitably chosen surfaces. Recently, rapid advances have been made in boosting their performance, but advancement in fundamental understanding has progressed more slowly. Currently, the most popular TENG models assume idealized flat surfaces that guarantee complete contact and a contact force (or load)-independent response. However, all real surfaces possess some level of surface roughness which is known to produce a load-dependent contact area. We develop a new unified model (for dielectric-to-dielectric TENGs) which adds consideration of surface roughness to the established distance-dependent electric field model. We account for surface roughness by applying Persson's contact theory to determine the load-dependent contact area. The model is applicable from first touch to nearly complete contact provided deformation remains elastic. Compared to load-independent approaches, the presented model is a better predictor of TENG performance. It captures the load-dependent nature of TENG performance apparent in recent tests. It predicts that the electrical output can be expected to be tiny at low contact loads, but should converge to an upper-bound at higher loads as the contact area approaches complete contact. Comparison with test results reveal substantially better prediction of open circuit voltage V_{OC} compared to load-independent models which tend to overestimate V_{OC} considerably. By assisting the designers with better predictions of TENG output, the developed unified theory has huge potential for advancing the use of TENGs in applications such as wearables (i.e. low loads) to tidal or wave energy (i.e. large loads).

1. Introduction

The modern triboelectric nanogenerator (TENG) is an energy harvester which utilizes contact electrification and electrostatic induction to transform kinetic energy into electricity [1,2]. Essentially, repeated cycles of contact of surfaces with sufficiently different electron affinities results in cycles of interfacial charge transfer, the generation of an electric field (during separation) and the ability to drive an alternating current. Over less than one decade of development, TENGs have been proposed as a viable energy harvester for a wide variety of applications (e.g. tidal energy [3], wearable sensors [4,5], electronic skin [6,7], medical technologies [8,9], etc.). Optimizing the output performance of TENGs has been a major priority to meet the energy requirements of these applications and most efforts so far have focused on trialing a range of judicious options for aspects such as surface texture [2], device materials [2,10], and environment [11], etc. Indeed, many of these efforts have led to modest performance improvements (such as a power density of 500 W/m^2) [12].

While device development has gained pace, the development of a fundamental understanding (or theory) of TENG operation has proceeded more slowly. The first theoretical TENG model was developed by Niu *et al.* [13] for a dielectric-dielectric TENG in contact-separation mode using the fundamental solution for the parallel flat capacitor. Niu *et al.* assumed that TENG devices have infinite lateral dimensions so that the electric field is constant between two oppositely charged plates (regardless of the distance between them). The voltage drop, V, induced charges on electrodes, Q, and the transient gap, $z(t)$, follow a strikingly simple first-order ordinary differential equation. Dharmasena *et al.* [14,15] abandoned the assumption of infinite sized TENG devices. Using the distance-dependent electric field associated with a finite rectangular

* Corresponding authors.
E-mail addresses: Ravinder.Dahiya@glasgow.ac.uk (R. Dahiya), Daniel.Mulvihill@glasgow.ac.uk (D.M. Mulvihill).

https://doi.org/10.1016/j.nanoen.2020.105067
Received 4 May 2020; Received in revised form 1 June 2020; Accepted 4 June 2020
Available online 9 July 2020

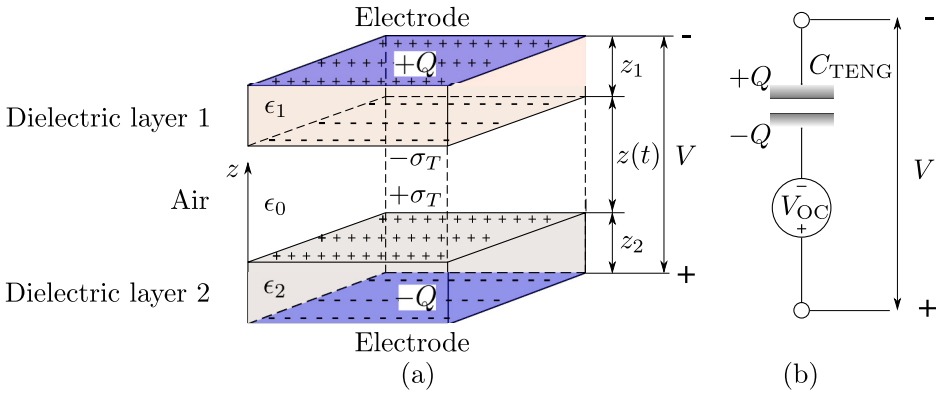

Fig. 1. (a) Schematic of a dielectric-dielectric type TENG device and (b) its lumped-parameter equivalent circuit model.

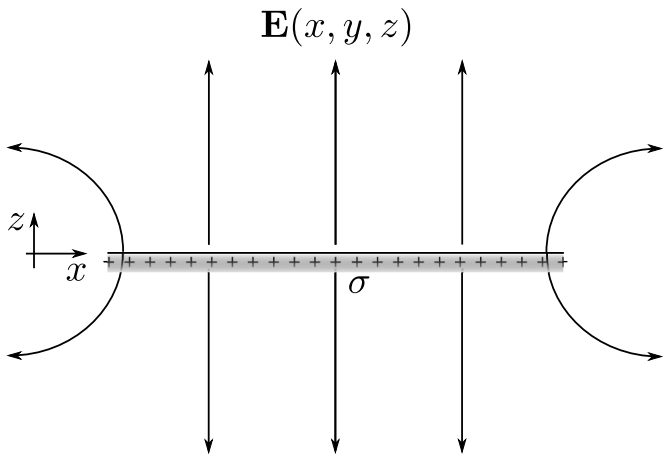

Fig. 2. Schematic of the $x-z$ cross-section of the electric field around a positively charged plate.

charged plate, Dharmasena *et al.* [14] developed a distance-dependent model that gave a better prediction. It was closer to the experimental result and crucially, it captured the saturation of open-circuit voltage at large separation. A similar model was derived by Shao *et al.* [16] where the electric field for a generalized TENG structure consisting of an arbitrary number of charged planes was given. Recently, a unified theory for a broader concept of nanogenerators (including TENGs) was derived by Wang [17] from Maxwell's equations. However, these simplified models do not capture the effect of real contact area and, as a result, they significantly over predict the open circuit voltage [14].

The models by Niu *et al.* [11] and Dharmasena *et al.* [14] do not account for the surface roughness, which means these models implicitly assume that charge transfer can occur over the full *nominal* device contact area A_n and that predicted electrical performance will be independent of the contact force. However, real surfaces always contain roughness and we know from decades of research in the field of contact mechanics, that roughness gives rise to a load-dependent *real* contact area A_r [18,19]. The real contact area is often tiny at low loads and can be expected to approach the nominal area at sufficiently high loads. This is important in the TENG scenario because it is reasonable to assume that charges might only transfer through areas of real contact. The implication being that increasing the load, and thereby the real contact area will increase tribo-charge density and thus increase the electrical output performance. The assumption that solid contact is required for tribo-electrification via electron tunneling has been verified by Li *et al.* [20] and Wang and Wang [21] who showed that the distance between approaching atoms across an interface must be within the equilibrium bond distance to enable electron transfer (i.e. within the interatomic repulsive regime).

Even though varying the contact load has not formed part of most studies, a few load-dependent TENG results have been published which point to this expected conclusion that, the higher the normal load, the better the electrical performance [22–29]. The first in-depth study of load-dependent TENG performance was done by Seol *et al.* [23]. Using a transparent glass slide in contact with a pyramid array textured polymer sheet, they found that the real contact area and V_{OC} all monotonically increase with the normal load until both are saturated at a certain contact pressure. A similar evolution of the real contact area between the glass and pyramid texture was also confirmed using computational methods [28,29]. Vasandani *et al.* [24] noted a linear increase in TENG voltage output with normal load in the low load range. Several attempts [24,28,29] have been made to adapt the load-independent TENG model [13] to be load-dependent. The nominal contact area within which tribo-charges distribute is replaced by the real contact area. Numerical methods [28,29] were used to calculate the real contact area – methods that could be used for any pair of interfaces. However, it is computationally expensive to run the numerical models, especially for those which require fine roughness details. Vasandani *et al.* [24] developed a load-dependent TENG theory using an asymptotic analytical solution [30] to approximate the real contact area between two non-textured nominally flat layers at low load conditions. However, this analytical solution can only accurately predict the real contact area when the contact ratio is small (<10%) [31]. In addition, this model is based on the earlier Niu *et al.* model [13] rather than Dharmasena *et al.* [14] – thus, it is based on the infinite parallel plate capacitor model which means voltage will not converge to a limiting value at high maximum separation distances (as is required in reality).

In this study, a new load-dependent TENG model is proposed to account for the presence of surface roughness in a dielectric-dielectric TENG in contact-separation mode. Our approach essentially adds the consideration of surface roughness to the distance-dependent electric field (DDEF) approach of Dharmasena *et al.* [14] by using Persson's contact theory [32] to account for a load-dependent real contact area covering the entire loading range from first touch to complete contact (Persson's contact theory gives a reasonable estimation of real contact area up to complete contact provided the deformation remains linearly elastic).

2. Existing theoretical models

2.1. The contact-separation mode TENG

Consider a dielectric-dielectric TENG as shown in Fig. 1(a). Two dielectric layers are subjected to periodic loading-unloading cycles with two dielectric surfaces in contact over the entire nominal contact area A_n. Permittivities of two dielectric layers and the air are ε_1, ε_2 and ε_0, respectively. The thicknesses of dielectric layers are z_1 and z_2,

respectively. The air gap is time-dependent and is represented by $z(t) \in [0, z_{max}]$. The tribo-charge, $\sigma_T A_n$, and induced charge, $Q = \sigma_U A_n$, are accumulated within the contact area and electrodes with constant densities, σ_T, and σ_U, respectively. The tribo-charge density is load-independent. The whole TENG device can also be represented (as in Fig. 1(b)) using a voltage source, V_{OC}, and a capacitor with charge, Q, and capacitance C_{TENG}.

A complete solution of the above problem can only be found numerically, but this is rather computationally expensive. An approximate approach proposed by Dharmasena *et al.* [14] is to simplify the TENG device into multiple parallel-flat charged plates. The TENG electric field is then the superposition of the electric fields of all charged plates. An implicit assumption behind this superposition is that the electric field of one charged plate is independent of the other charged plates.

The theoretical TENG models aim to establish the relationship between the voltage drop over the TENG, V, induced charges on the electrode, Q, and the transient air gap, $z(t)$. Most of the existing theoretical models can be summarized into one general formulation which will be given in Section 2.2. Finally, some representative models which can be naturally deduced from the general formulation are given as examples in Section 2.3 and 2.4.

2.2. General formulation

As the building block of the whole formulation, let us revisit the electric field around a charged plate first. Consider a positively charged plate occupying an arbitrarily shaped region Ω on the $z = 0$ plane. The charge density on the plate is σ. The surrounding is isotropic and homogeneous with a constant permittivity ε. The electric field is in a vector form, $\boldsymbol{E}(x, y, z)$, see Fig. 2. Since the voltage drop across the thickness of the TENG device matters, only the electric field in the z-direction is considered, i.e. $E_z(x, y, z) = E_z(x, y, -z)$. Commonly, the through-thickness dimension in TENG devices is much smaller than the lateral dimensions. Therefore, we can use the following step function to simplify $E_z(x, y, z)$

$$E_z(x,y,z) = \begin{cases} \dfrac{\sigma}{\pi\varepsilon} f(z) & (x, y) \in \Omega \\ 0 & (x, y) \notin \Omega \end{cases} \tag{1}$$

This approximation indicates that the electric field in the vertical direction is uniform within the projected area of the charged plate for a given z and instantaneously drops to zero outside. An example of $E_z(x, y, z)$ associated with a circular disc can be found in Appendix A. Based on the above electric field for a single charged plate, we can determine the electric field and resulting electrical outputs of the TENG device:

2.2.1. Open-circuit voltage V_{OC}

The open-circuit voltage between two electrodes is related to the two charged plates with tribo-charges, $\pm\sigma_T$, alone and can be written as $V_{OC} = V_{+\sigma_T} + V_{-\sigma_T}$ where $V_{+\sigma_T}$ and $V_{-\sigma_T}$ are the voltage drops due to positive and negative tribo-charges. Using the definition of the voltage: $V = -\int E_z(z)\, dz$, we can have V_{OC} in an integral form:

$$V_{OC} = \frac{\sigma_T}{\pi}\left\{2\varepsilon_0^{-1}\int_0^{z(t)} f(z)dz + \varepsilon_1^{-1}\left[\int_{z(t)}^{z(t)+z_1} f(z)dz - \int_0^{z_1} f(z)dz\right] + \varepsilon_2^{-1}\left[\int_{z(t)}^{z(t)+z_2} f(z)dz - \int_0^{z_2} f(z)dz\right]\right\} \tag{2}$$

2.2.2. Voltage drop V

The voltage drop V is composed of the contributions from the charged plates with induced charges $\pm\sigma_U$ and tribo-charges $\pm\sigma_T$, i.e. $V = V_{+\sigma_U} + V_{-\sigma_U} + V_{OC}$:

$$V = -\frac{\sigma_U}{\pi}\left(\varepsilon_1^{-1}\left[\int_0^{z_1} f(z)dz + \int_{z_2+z(t)}^{z_1+z_2+z(t)} f(z)dz\right] + \varepsilon_0^{-1}\left[\int_{z_1}^{z_1+z(t)} f(z)dz + \int_{z_2}^{z_2+z(t)} f(z)dz\right] + \varepsilon_2^{-1}\left[\int_{z_1+z(t)}^{z_1+z_2+z(t)} f(z)dz + \int_0^{z_2} f(z)dz\right]\right) + V_{OC} \tag{3}$$

2.2.3. Short-circuit charges Q_{sc}

Letting $V = 0$ in Eq. (3), we directly obtain the short circuit charges

$$Q_{sc} = A_n\sigma_U = V_{OC}C_{TENG} \tag{4}$$

where C_{TENG} is the equivalent capacitance of the TENG device

$$C_{TENG} = A_n\pi \Bigg/ \left(\varepsilon_1^{-1}\left[\int_0^{z_1} f(z)dz + \int_{z_2+z(t)}^{z_1+z_2+z(t)} f(z)dz\right] + \varepsilon_0^{-1}\left[\int_{z_1}^{z_1+z(t)} f(z)dz + \int_{z_2}^{z_2+z(t)} f(z)dz\right] + \varepsilon_2^{-1}\left[\int_{z_1+z(t)}^{z_1+z_2+z(t)} f(z)dz + \int_0^{z_2} f(z)dz\right]\right) \tag{5}$$

2.3. Model of Niu et al. [13]

The most prevalent model thus far in TENG design is that of Niu *et al.* [13] They assumed the lateral dimensions of the TENG to be infinite. This assumption is valid when the maximum gap, z_{max}, is significantly smaller than the lateral dimensions. Based on the classic solution of the parallel flat capacitor, $f(z)$ in Eq. (1) has a simple solution: $f(z) = \pi/2$. Substituting this value of $f(z)$ into Eqs. (2), (3) and (5), we deduce the strikingly simple equations [13]:

$$V = -\frac{Q}{A_n\varepsilon_0}\left[\varepsilon_{r1}^{-1}z_1 + z(t) + \varepsilon_{r2}^{-1}z_2\right] + V_{OC} \tag{6}$$

$$V_{OC} = \frac{\sigma_T z(t)}{\varepsilon_0} \tag{7}$$

$$C_{TENG} = \frac{A_n\varepsilon_0}{\varepsilon_{r1}^{-1}z_1 + z(t) + \varepsilon_{r2}^{-1}z_2} \tag{8}$$

2.4. Model of Dharmasena et al. [14]

Dharmasena *et al.* [14] abandoned the infinite flat plate assumption used in Niu *et al.* [13] Based on a finitely sized rectangular-shaped device (L: length and W: width), they found the corresponding $f(z)$ as:

$$f(z) = \arctan\left(\frac{L/W}{2(z/W)\sqrt{4(z/W)^2 + (L/W)^2 + 1}}\right) \tag{9}$$

Taking $L,\ W\rightarrow\infty$, Eq. (9) approaches $\pi/2$. To simplify the development of our load-dependent model, we assume an equivalent circular TENG device of radius, a, which has the equivalent electrical performance as the rectangular one. This just results in a simpler expression for $f(z)$ which simplifies the development of the load-dependent model in Section 3. This time, the corresponding function $f(z)$ takes the following axisymmetric form:

$$f(z)=\frac{\pi}{2}\left(-\frac{z}{\sqrt{A_n/\pi+z^2}}+1\right) \tag{10}$$

A numerical example is given in Appendix B and shows that Eq. (10) and Eq. (9) are almost the same given the same nominal area, i.e. $\pi a^2 = L\times W = A_n$. Similarly, the above $f(z)$ has an asymptotic limit of $\pi/2$ as $A_n\rightarrow\infty$ (or $z\rightarrow 0$).

For fixed L and W, this asymptotic limit can also be reached if the separation z is negligibly small. Therefore, we should expect that the model of Dharmasena *et al.* [14] should eventually converge to the model of Niu *et al.* [13] at small maximum separation, z_{max}. However, we find the formulations in Eqs. (8)–(10) of Dharmasena *et al.* [14] to be incomplete. The permittivity of the air is missing. This will cause an underestimation of V_{OC} and it will fail to converge to the model of Niu *et al.* [13] at small z_{max}. In Fig. 2(e) of reference [16], this is clearly visible as a gap between the Niu *et al.* model and the Dharmasena *et al.* model (at low z_{max}). An improved approach is to use the general formulations described here in Eqs. (2)–(5) above (where the permittivity of the air is now included). We refer to the model incorporating this correction and using $f(z)$ from Eq. (10) as the *modified Dharmasena et al. model*. Using the TENG device in Ref. [14], Fig. 3 compares the predicted V_{OC} for the modified Dharmasena *et al.* model described here with the original Dharmasena et al. and Niu *et al.* models. It is clear in Fig. 3 that the modified Dharmasena *et al.* model now converges to the Niu *et al.* model at a small separation distance.

3. Load-dependent model: Theory

In the Niu *et al.* and Dharmasena *et al.* models in Section 2, tribo-charges are assumed to be uniformly distributed over the entire dielectric surface (i.e. over the entire nominal contact area A_n). However, in practice, the inevitable presence of surface roughness means that complete contact between dielectric surfaces is hardly ever achieved. Instead, we can expect that tribo-charges might only exist on the real contact area A_r which is load-dependent and composed of an array of randomly distributed irregularly shaped spots — see the experimental result produced using pressure sensitive film in Fig. 4(a–c). A measured example of load-dependent real contact area is also given in Fig. 4(d) to illustrate the commonly measured monotonic increase in real contact area with contact force [19]. Consequently, all models discussed in Section 2 are only applicable as the asymptotic TENG model when the contact load is sufficiently large to achieve a complete contact. Note, if one of the tribo-contact layers were a conductor (i.e. dielectric-to-conductor type TENG), the tribo-charges could be expected to distribute over the entire nominal area and this would require a somewhat different formulation to the one set out here.

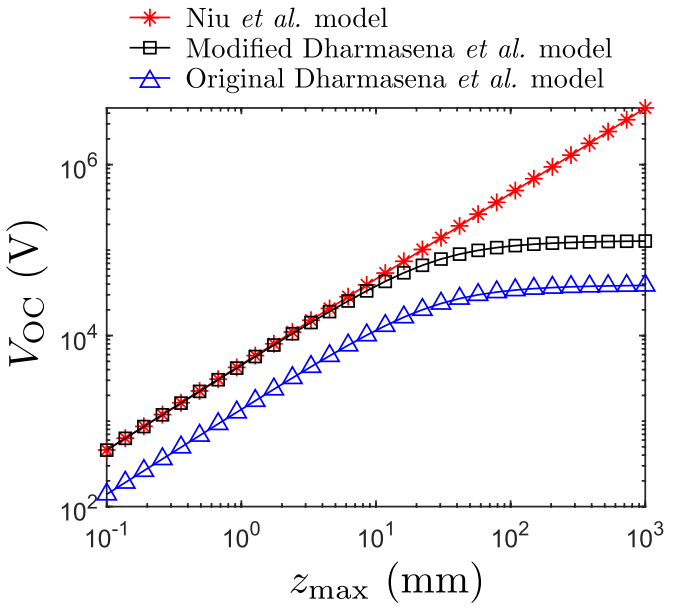

Fig. 3. Open-circuit voltage prediction versus separation distance comparing the modified Dharmasena *et al.* model described here with the Niu *et al.* model [13] and the original Dharmasena *et al.* model [14]. TENG device parameters are from Ref. [14]. The tribo-charge density is 40.7 $\mu C/m^2$. Note: at low separation distances, Niu *et al.* [13] and modified Dharmasena *et al.* (present work) are now in agreement.

The load-dependent TENG model proposed in this section is extended from the modified Dharmasena *et al.* model discussed in Section 2.4. We will divide model development into two parts: the contact stage and the separation stage.

3.1. Contact stage

During the contact stage, two nominally flat randomly rough dielectric surfaces are pressed into purely normal contact by a normal load F - see Fig. 5.

Crucially, in this study, we use Persson's contact theory [32] to determine the load-dependent real contact area. The real contact area, A_r, in Persson's contact theory is expressed as an error function of the normal load

$$\frac{A_r}{A_n}=\mathrm{erf}\left(\frac{F}{A_nE^*}\sqrt{\frac{2}{|\nabla h_1|^2+|\nabla h_2|^2}}\right) \tag{11}$$

where $h_1(x,\ y)$ and $h_2(x,\ y)$ are the heights of two dielectric surfaces, $\langle f\rangle$ represents the average of f over the entire nominal contact area and E^* is the composite modulus:

$$\frac{1}{E^*}=\frac{1-\nu_1^2}{E_1}+\frac{1-\nu_2^2}{E_2} \tag{12}$$

where E_i and ν_i ($i=1,\ 2$) are the Young's modulus and Poisson's ratio of two dielectric layers, respectively. Note that Persson's contact theory in Eq. (11) only applies for linear elastic materials. Persson's theory shows a monotonic increase of A_r with respect to the normal load until $A_r\rightarrow A_n$ when $F\rightarrow\infty$. Therefore, the area where the tribo-charges distribute can only be determined by Eq. (11) with $F=F_{max}$ where F_{max} is the maximum normal load in one periodic cycle. The advantage of using Persson's contact theory (as opposed to other approaches for calculating contact area such as those based on the Greenwood and Williamson model [33]) is that it remains applicable approaching complete contact provided the deformation remains linearly elastic. For the compliant polymers used as TENG interfaces, it is reasonable to assume elasticity up to high contact ratios. Using Persson's contact theory means that the model is applicable to a far wider range of contact loads as opposed to the approach taken in developing the Vasandani *et al.* [24] load-dependent model which is only valid for contact ratios less than about 10% [31].

$|\nabla h_1|$ and $|\nabla h_2|$ in Eq. (11) are the surface gradients of the two contact surfaces and Persson's contact theory requires the assumption that the root mean square (RMS) surface gradient is small – i.e. that:

$$\sqrt{|\nabla h_i|^2}=\sqrt{|\partial \mathrm{h_i}/\partial \mathrm{x}+\partial \mathrm{h_i}/\partial \mathrm{y}|^2}<1\quad i=1,\ 2 \tag{13}$$

Most TENG surfaces will be sufficiently smooth for this to be a valid assumption (see Table C1 in Appendix C) where the mean RMS surface

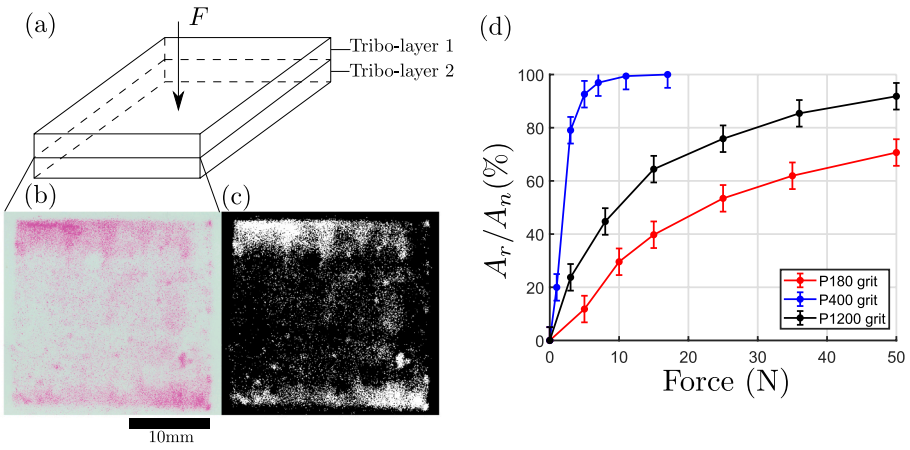

Fig. 4. (a) Schematic illustration of two tribo-layers in normal contact; (b) Measurement of the real contact area between two tribo-layers using pressure-sensitive film, red: contact spot; (c) Binarized image of (b) white: contact area. Contact ratio here is 20.84%; Normal load: 150 N; Tribo-layer 1: Cu electrode and tribo-layer 2: PET film. Layer size: 25 × 25 mm^2; (d) The real contact area between PDMS surfaces with different roughness and glass. (d) is adapted from Refs. [19] with permission from Elsevier.

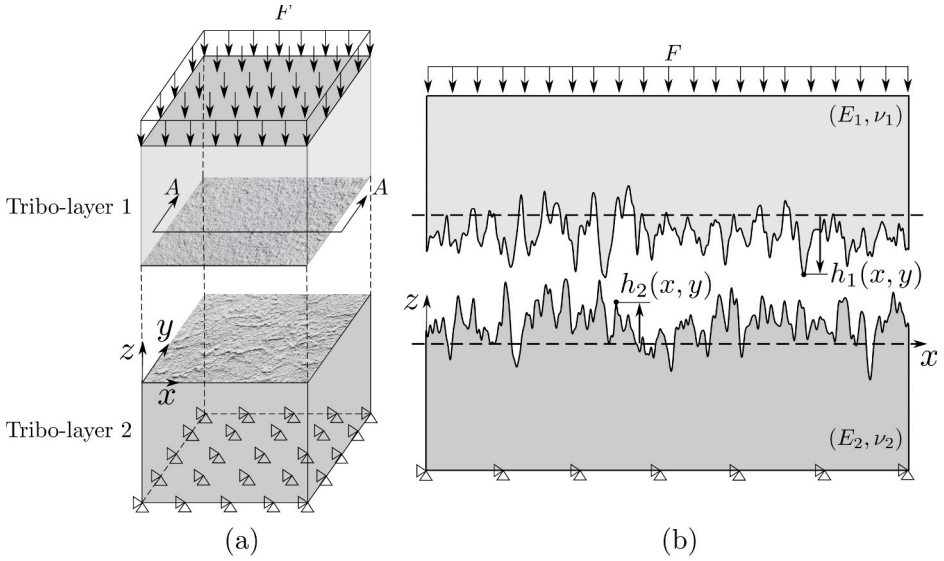

Fig. 5. Schematic illustration of: (a) two rough layers in purely normal contact and (b) the cross-sectional view on the $x - z$ plane.

Table 1
TENG design parameters [14]. The permittivity of air is $\varepsilon_0 = 8.85 \times 10^{-9} \mu F/mm$. The permittivity of the bottom layer is calculated by Eq. (S15) of [14].

Tribo-charges density ($\mu C/m^2$)	40.7	Material	Relative permittivity	Thickness (mm)
Top layer	Tribo-layer	PET	3.3	0.2
Bottom layer	Tribo-layer	PDMS	2.72	0.02
	Substrate	PET	3.3	0.2

gradient for PDMS and PET was 0.13 and 0.17, respectively). Eq. (13) guarantees that the upper limit of the real contact area is approximately the nominal contact area, i.e. $A_r \rightarrow A_n$ when the normal load, F, is sufficiently large.

3.2. Separation stage

A complicated electric field is created in the TENG device once two rough dielectric layers are separated due to the separated and random distribution of the tribo-charges on the dielectric surface. The true electric field can only be determined using numerical methods, (e.g. finite element method). To reduce the computational complexity, we propose a simple approximation. Essentially, we assume the electric field produced by the distributed tribo-charge spots to be nearly equivalent to that produced by a single disc having the same total area of tribo-charges. Fig. 6 illustrates the simplification. Thus, assigning radius a' to the equivalent disc, we require $\pi(a')^2 = A_r$.

Then, instead of solving Fig. 6(a), the simpler problem in Fig. 6(b) is solved with the assumption that both models result in very similar voltage drop V and induced charge Q. Detailed discussions on the accuracy of this approximation are given in Section 4.3.

Assuming the induced charges are still uniformly distributed over the disc, the general formulation, in Eqs. (3)–(5) can still be used here and, thus, V_{OC} in Eq. (2) is adapted to include the effect of rough surface contact. Since the electrode and charged disc of radius a' are concentric, the electric field, $E_z(r, z)$, due to the charged disc over the electrode is no longer uniform. An example can be found in Appendix B. Thus, an average electric field over the entire electrode is defined as

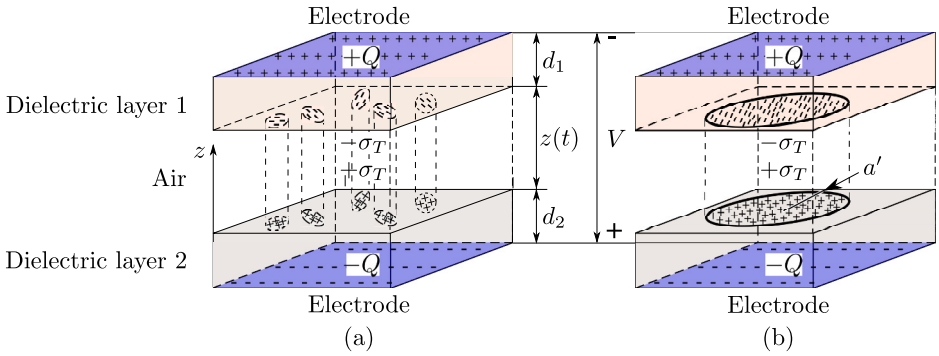

Fig. 6. Schematic illustration of the circular TENG simplification: (a) with a discretized distribution of tribo-charges and (b) with a concentrated distribution of tribo-charges within a concentric circular area.

$$\overline{E}_z(z) = \frac{\sigma_T}{\pi} f'(z) \tag{14}$$

where

$$f'(z) = \frac{\pi}{2}\left[-\frac{z}{\sqrt{A_r/\pi + z^2}} + 1 \right] \left(\frac{A_r}{A_n}\right)^2 \tag{15}$$

A new formulation of V_{OC} is then achieved by replacing $f(z)$ with $f'(z)$ in Eq. (2). As normal load $F \to \infty$, $A_r \to A_n$ and $f'(z) \to f(z)$ and the load-dependent model converges (as required) to the modified Dharmasena *et al.* model from Section 2.4. A complete summary of the load-dependent TENG model is given in Appendix E.

4. Load-dependent model: Results and discussion

4.1. Comparison with previous models and test data

To apply the load-dependent model to a real TENG scenario, we use the example in Dharmasena *et al.* [14] where test data is available for comparison. The TENG in Dharmasena *et al.* [14] is a dielectric-dielectric device in contact-separation mode. It is composed of a polyethylene terephthalate (PET) film and a polydimethylsiloxane (PDMS) coated PET film. At the contact interface, PET contacts the PDMS coating. The nominal contact area was a square having $L = W =$ 50 mm. For our purposes, this is equivalent to a circular disc of radius $a \approx$ 28.21mm. We use this radius for the modified Dharmasena et al. model (Section 2.4) and the load-dependent model (Section 3). The two dielectric layers undergo periodic loading and unloading with a sinusoidal motion: $z(t) = \frac{z_{max}}{2}[1 - \cos(2\pi f t)]$ where $f = 1$ Hz. Although Dharmasena *et al.* [14], did not report surface roughness information, we have characterized the surface topography of similarly produced PET and PDMS surfaces (the samples used for the load-dependent testing in Section 4.2) - details are given in Appendix C. This information (in particular the composite RMS surface gradient in Table 2) is required for the rough surface contact modeling. Note that we use the tribo-charge density of $\sigma_T = 40.7\ \mu C/m^2$ as an input to the model as we are using exactly the same material pair as in Ref. [14]. Design parameters of the TENG and the parameters required for the contact simulation are summarized in Tables 1 and 2

Table 2
Parameters related to contact mechanics modeling. Calculation of the composite RMS surface gradient can be found in Eq. (C.1) in Appendix C.

Contact pair	Young's modulus (MPa)	Poisson's ratio	Composite RMS surface gradient
			$\sqrt{\lvert\nabla h_1\rvert^2 + \lvert\nabla h_2\rvert^2}$
PET	2.35×10^3 [34]	0.4 [34]	0.2159
PDMS	1.4 [35]	0.48 [36]	

Based on this TENG configuration, we now compare the load-dependent model to the load-independent models and to the experimental result reported in Dharmasena *et al.* [14]. Returning to the derivation of the load-dependent electrical outputs, using Ohm's law, $V = I \times R = \frac{dQ}{dt}R$, we can rewrite Eq. (3) as a first-order ordinary differential equation:

$$R\frac{d}{dt}Q = -\frac{Q}{C_{TENG}} + V_{OC} \tag{16}$$

where $Q = A_n\sigma_U$ is the total induced charges on electrodes and C_{TENG} and V_{OC} take the forms in Eqs. (5) and (2).

The first order ordinary differential equation, Eq. (16), is then solved using *ode15s*() in MATLAB®. Fig. 7(a–c) shows how the load–dependent model affects transient electrical outputs V, V_{OC} and I_{SC} (for one cycle) as compared to the modified Dharmasena *et al.* model. Results are plotted for five loading cases (8, 32, 128, 512 and 800 N). The plots in Fig. 7 (a–c) demonstrate the highly load-dependent nature of the electrical outputs: V, V_{OC} and I_{SC} all increase with normal load. This is a direct consequence of the load-dependent real contact area associated with rough surface contact. This is clear from Fig. 7(d) where we see real contact area also increasing with normal load according to Persson's theory. Commonly, TENG tests are conducted on centimeter sized nominal areas with normal loads less than about 20 N and, without special texturing, it is rare to measure thousands of Volts for V_{OC} as predicted by the load-independent model (e.g. modified Dharmasena *et al.*). We know from several experimental studies in tribology [18,19] that real contact area is load-dependent and a few studies to date [22–29] have shown a similar load dependence in the electrical output of TENGs. Therefore, Fig. 7 clearly suggests that the overestimation of electrical performance by the existing (load-independent) models is likely to be due to the assumption of complete contact.

Maximum voltage V_{max}, and maximum current I_{max}, are plotted with respect to normal load (1 N–1800 N) in Fig. 8(a) and Fig. 8(b), respectively. V_{max} and I_{max} experience initial rapid growth followed by a slow asymptotic transition to the modified Dharmasena *et al.* result (horizontal dashed lines in Fig. (8) at higher loads. A similar trend can also be observed for the real contact area predicted by Persson's contact theory in Fig. 7(d). A_r initially increases rapidly with normal load and then asymptotically approaches the limiting nominal contact area A_n at sufficiently high loads. Thus, it is clear that the existence of a limit on TENG electrical output is determined by the corresponding limiting real contact area. The modified Dharmasena *et al.* model corresponds to the limiting electrical output because this model is derived based on the assumption of complete contact. The predicted existence of a limit for TENG output is important as it provides an upper-bound for the performance of a given tribo-contact pair.

Electrical output in the load-dependent model is entirely determined by normal load. It can be tiny at low loads and reaches a maximum at a

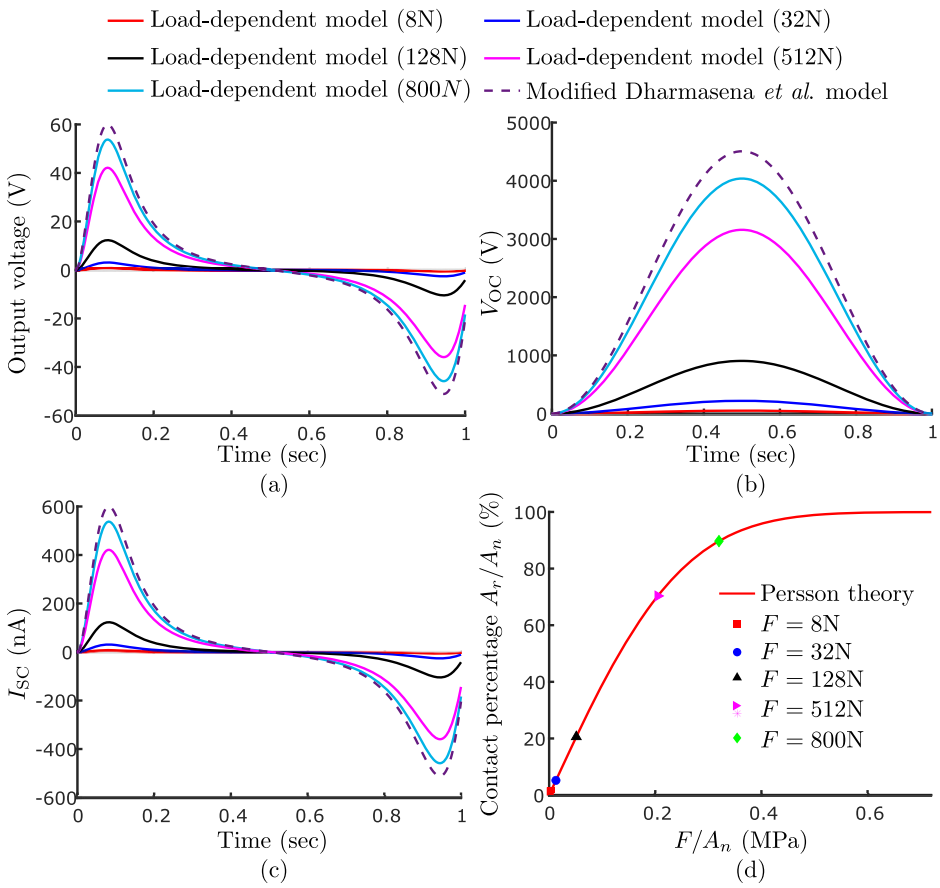

Fig. 7. Transient electrical performance of TENG in the first cycle: (a) output voltage with $R = 100\,M\Omega$, (b) V_{OC}, (c) I_{SC}, and (d) the corresponding Persson prediction of the real contact area. Normal load range: $F \in [1\text{ N},\ 1800\text{ N}]$. $z_{max} = 1$ mm.

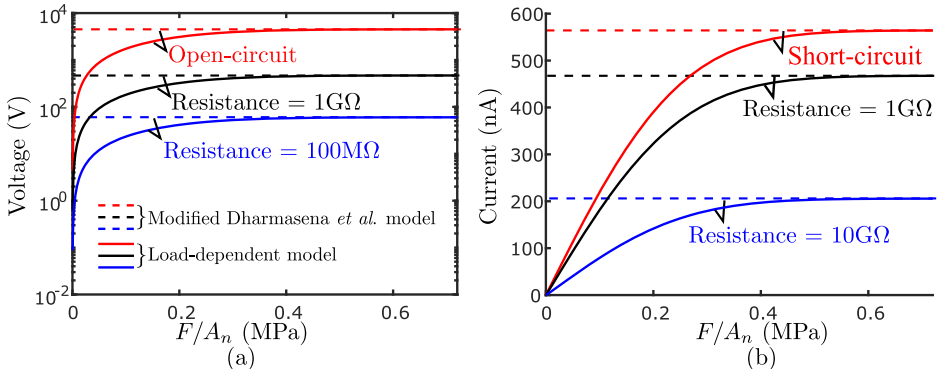

Fig. 8. (a) Maximum voltage and (b) maximum current vs. normal load normalized by A_n. $z_{max} = 1$ mm.

load corresponding to nearly complete contact. Increasing the normal load from 1 N to 1800 N, the electrical output shown in Fig. 8 (i.e. maximum voltage or current) can have more than a two orders of magnitude increase. Clearly load dependence is a critical aspect for TENG designers to consider as TENG output will depend strongly on the normal load pressing the surfaces together - especially in the low load range were sensitivity to load is greatest. An attempt to predict device output for a given loading scenario using load-independent models is likely to seriously overestimate electrical output without consideration of the load-dependent rough surface behavior captured here. In particular, in the low load range (<100 N or 0.04 MPa here), TENG output is highly sensitive to load and there is scope for large error if the load-dependent nature of the contact is not very carefully considered.

Maximum voltage and maximum current in the first loading period associated with different external resistance R are shown in Fig. 9(a) and (b). The evolution of power $P = I_{max}^2 R$ with respect to the external resistance R can be found in Fig. 9(c). The optimized resistance associated with the peak value of the power in Fig. 9(c) can be correlated with the normal load in Fig. 9(d). As required, regardless of the normal load, V_{max} gradually saturates (i.e. to V_{OC}) as $R \to \infty$. Similarly, I_{max} slowly converges to I_{SC} as $R \to 0$. Fig. 9(d) indicates that optimized resistance predicted by the load-dependent model increases somewhat with increasing load – this is likely due to the increasing real contact area

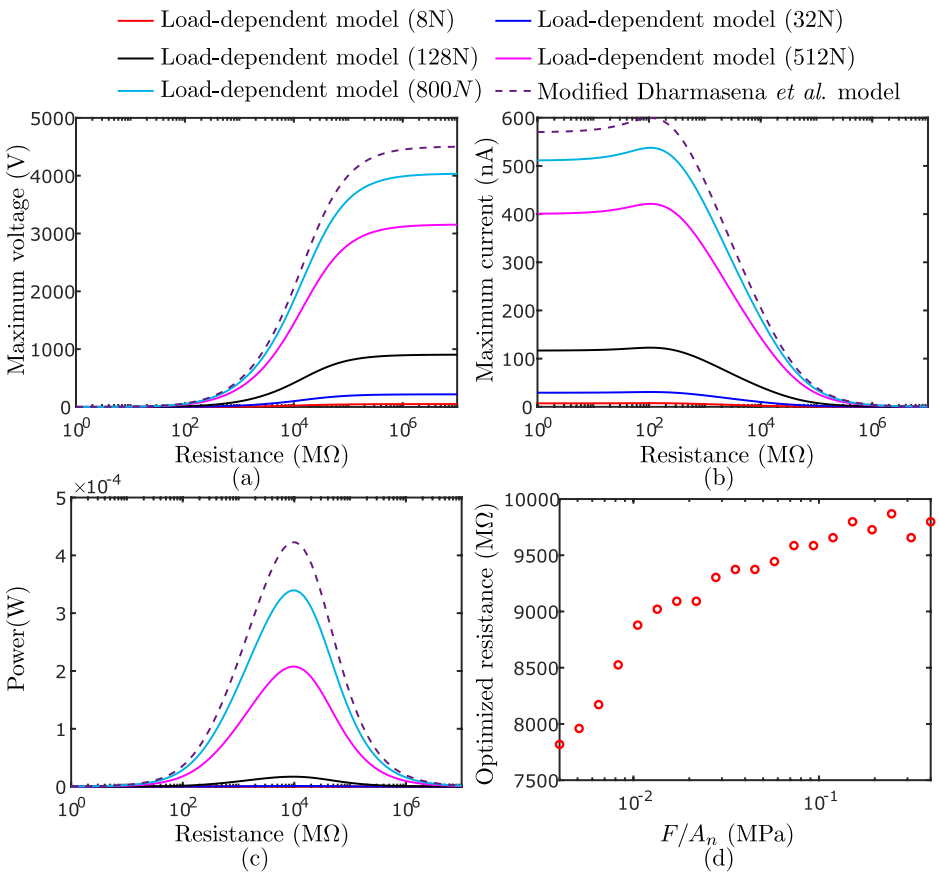

Fig. 9. (a) Maximum output voltage, (b) Maximum output current and (c) the corresponding power vs. resistance. (d) Variation of optimized resistance with respect to resistance. Normal load range in (d): $F = [1\text{ N}, 1000\text{ N}]$. $z_{max} = 1$ mm.

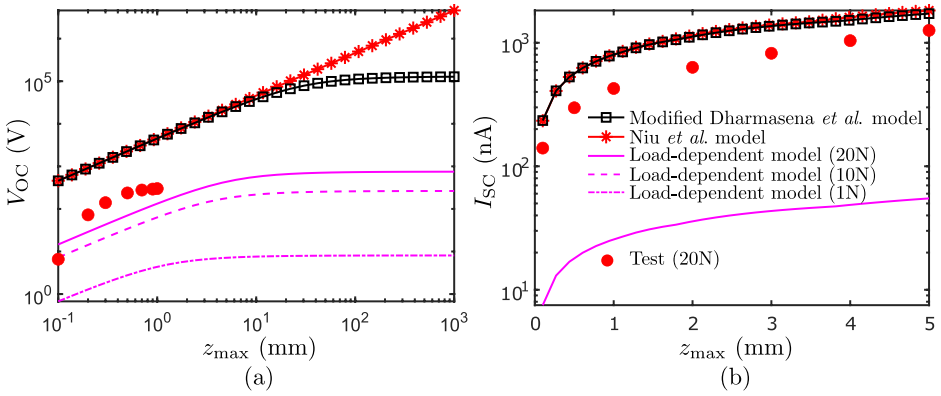

Fig. 10. (a) $V_{OC}$and (b) I_{SC} predicted by theoretical models and the corresponding test data. The test was performed under the normal load of 20 N.

with normal load (Fig. 7(d)). Optimized resistance is more sensitive to normal load at low loads and less sensitive at higher loads. This sensitivity is due to the fact that the maximum voltage and maximum current grow more rapidly in the low load regime, see Fig. 8. As normal load decreases from 1000 N to 1 N in Fig. 9(d), the optimized resistance decreases by approximately 20%. This drop can be explained by the fact that the maximum voltage associated with lower normal load converges to its maxima at smaller resistance, see Fig. 9(a). However, the peaks in Fig. 9(c) show that the optimized resistance varies within a tight band compared with the logarithmic scale of resistances.

In Fig. 10, we plot the load-dependent predictions alongside the Niu *et al.* and modified Dharmasena *et al.* models. The experimental data [14] carried out at a contact load of 20 N is also plotted. As we pointed out in Section 2.4 the original Dharmasena *et al.* model contains an inconsistency which causes its V_{oc} prediction to fail to converge to the model of Niu *et al.* [13] at small z_{max} – this is visible in Fig. 2(e) of Shao *et al.* [16]. This problem is corrected here in the modified Dharmasena *et al.* model which now converges to Niu *et al.* as z_{max} approaches zero as Fig. 10(a) shows.

The Dharmasena *et al.* [14] model (and the modified version presented here) produce an open circuit voltage V_{OC} which rightly saturates at sufficiently high maximum separation z_{max}. Therefore, the load-dependent model (which uses the same distance-dependent electric field approach) also converges to a saturated V_{OC} at high separations as Fig. 10(a) shows. However, the Dharmasena *et al.* model and the Niu *et al.* model significantly overestimate V_{OC} and this is likely due to the

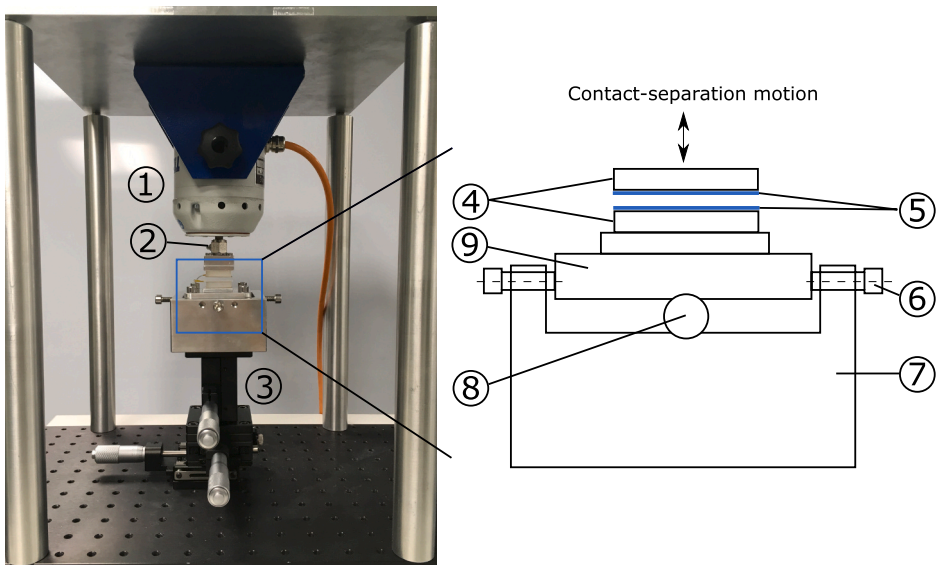

Fig. 11. (a) TENG test rig and (b) Schematic illustration of flat-on-flat contact between two dielectric layers using a customized self-aligning platform. (1) Electrodynamic shaker; (2) Load sensor; (3) Manual *xyz* stages; (4) Glass plates; (5) dielectric layers of TENG device; (6) Lock screws; (7) housing of self-aligning platform; (8) Bearing ball of diameter 10 mm; (9) Self-aligning platen.

impractical assumption of ideally smooth surfaces producing complete contact. An average relative difference of 20 times with a maximum of 70 times is observed between the test results and all load-independent models. Among all theoretical models, the load-dependent model with $F = 20$ N has the closest agreement with the test data. It only underestimates V_{OC} by an average difference of 2.5 times with a maximum of 3.4 times. Although it is hard to be sure, the experimental V_{OC} data in Fig. 10(a) appear to be saturating by about 1 mm separation. The load-dependent model (at $F = 20$ N) saturates far closer to this point than the load-independent models and also appears to be converging to a very similar value of V_{OC}. Thus, the load-dependent model improves the prediction of the voltage-separation evolution significantly.

All models in Fig. 10(b) show considerable disagreement with the test data for I_{SC}. The reason for this is not entirely clear, but based on the results in Dharmasena *et al.*, it appears to be difficult to find simultaneous agreement with test data for *both* V_{OC} and I_{SC} [14]. Discussion of possible reasons for differences between model and experiment are discussed in Section 4.3 below.

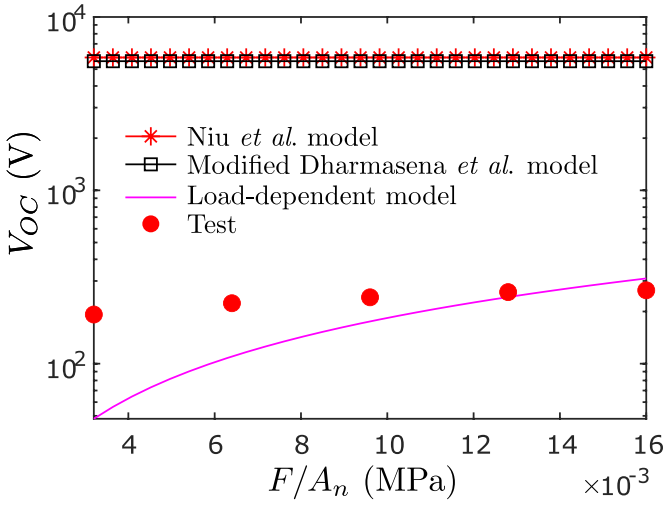

Fig. 12. V_{OC} versus normal load comparing test data to load-dependent and load-independent models. Normal load range: $F = [2\text{ N},\ 10\text{ N}]$.

4.2. Comparison with load-dependent test

The test in Dharmasena *et al.* (and plotted in Fig. 10 above) was for a single contact load of 20 N [14]. To investigate load dependence experimentally, we conducted a load-dependent test using the same tribo-contact material pair as Dharmasena *et al.* (i.e. PET and PDMS). The test rig designed for the work is shown in Fig. 11(a). An electrodynamic shaker (1) was used to produce the TENG oscillation and the upper and lower layers of the TENG device (5) where glued to ultra-smooth, high flatness optic glass plates (4). Since we are concerned with load-dependent contact behavior, it is essential to ensure good conformity between the tribo-surfaces during contact. Otherwise, if two flat layers are not perfectly parallel, contact may be localized at the edges. Indeed Hong *et al.* found that V_{OC} dropped by nearly 75% for a misalignment of 1° [37]. This important experimental point has often been overlooked in the literature. Therefore, a bespoke self-alignment mechanism (Fig. 11(b)) was designed to ensure pre-test alignment of the surfaces. The upper plate is fixed, but the lower plate is free to rotate (prior to the test) on a ball bearing (8). Initially, the surfaces are brought into contact under a pre-load to self-align and then the plates are locked in position for the test using lock screws (6). The separation distance z_{max} was fixed at 1.3 mm and a sinusoidal oscillation was applied at $f = 8$ Hz. The nominal contact area was 25 × 25 mm^2. Surface roughness measurements on the samples are discussed in Appendix C. More details of the test and specimen fabrication can be found in Appendix D.

The test result is plotted alongside the load-dependent model and the load-independent models (modified Dharmasena *et al.* and Niu *et* al.) in Fig. 12. As in Fig. 10(a), the load-dependent model shows the best accuracy among all models. All load-independent models have a constant prediction of V_{OC} which differs from the test data by more than one order of magnitude while the load-dependent model is much closer in magnitude to the test data. Both the load-dependent model and the test result show an increasing trend with contact load. However, the model simulates a more dramatic increase than the test data here. The test data does increase from 192 V to 265 V in Fig. 12, but this is less obvious with the logarithmic scales. We explore possible reasons for such disagreement with test data in Section 4.3.

4.3. Remarks on agreement between model and experiment

It is clear that the load-dependent model accounting for surface roughness produces a much more accurate description of experimentally observed TENG behavior than load-independent models. However, as we have seen, there are still some discrepancies between model and experiment.

In Fig. 10(b), we saw that the load-dependent I_{SC} significantly underestimates the measured value by at least one order of magnitude, while V_{OC} agrees quite closely with the test data. Therefore, since $I_{SC} = \frac{d}{dt}Q_{SC} = \frac{d}{dt}(C_{TENG}V_{OC})$, we may conclude that C_{TENG} may be underestimated in the load-dependent model. We can also expect that this may result in an underestimation of the output current, output voltage and power when the TENG is connected to external resistance. We notice in particular from the form of Eq. (5) above that C_{TENG} (in the model) is actually load-independent. This may be caused by the simplified superposition principle used whereby the electric fields of four charged surfaces (the two tribo-contact surfaces and two electrodes) are combined on the assumption of being completely decoupled from each other. This conclusion also applies to the load-independent models. As noted already, it appears to be difficult to achieve good agreement with experiment for both I_{SC} and V_{OC}. For example, Dharmasena *et al.* [14] had agreement (at one fixed normal load) for I_{SC} but not for V_{OC}. Finding agreement for both remains an open challenge. One suggestion is to modify the present load-dependent TENG model so that the capacitance of the TENG can be directly measured or estimated using advanced multi-physics FE models accounting for both rough surface contact and electro-statics. While the predicted magnitudes of power and optimized resistance in Fig. 9 will, of course, depend on I_{SC}, the overall trends remain the same: the key trend being that electrical output increases monotonically with the load pressing the surfaces together.

Also, the accuracy of V_{OC} itself may be limited by the idealized contact mechanics model. This could be improved by considering more refined aspects such as plastic deformation; rate and history-dependent deformation; electro-adhesion and the thin layered nature of the flat-on-flat contact in TENGs (i.e. the materials at the interface are not elastic half-spaces but thin layers). Another important factor affecting agreement with experiments will be the accuracy of the tribo-charge density σ_T used as an input to the models. Accurate measurement (and prediction) of σ_T is an area requiring extensive further investigation so that models can use the most accurate value available.

5. Conclusions

A unified load-dependent triboelectric nanogenerator (TENG) model which accounts for the inevitable presence of surface roughness on TENG contact surfaces has been developed (for dielectric-to-dielectric TENGs in contact separation mode). Crucially the model accounts for the well-known load-dependent *real* contact area that results from the contact of multiscale rough surfaces. The model uses Persson's contact theory to determine the contact area and is therefore applicable to contact from first touch up to nearly complete contact (i.e. near 100% contact) as long as deformation remains elastic. The model results in a load-dependent TENG electrical performance – something which has been noted experimentally in recent literature. Voltage, current and power all increase with contact force until the contact area saturates. To determine the electric field, the model uses a modified version of the distance-dependent electric field model (Dharmasena *et al.* [14]). This guarantees that voltage output in the load-dependent model saturates at high separation distances. We also add a modification which now allows the distance dependent model to converge to the distance independent infinite parallel plate capacitor model (Niu *et al.* [13]) at low separation distances. As required, the model also converges to the load-independent model of Dharmasena *et al.* [14] at contact forces sufficient to saturate the contact area (i.e. at near 100% contact). The load-independent Dharmasena *et al.* model therefore represents an important upper bound on the performance. The model presented here is a better predictor of the experimentally observed TENG performance than previous models in that it captures the load-dependent behavior, is applicable over a far wider range of contact forces and predicts an open circuit voltage considerably closer to the test data. There is still further scope for refinement as short circuit current was underestimated by the model – a number of possibilities for future refinement were given in Section 4.3.

Load-dependence leads to some important implications and possibilities. For example, a load-dependent TENG could be used as a pressure sensor – e.g. in vehicle tires or in weigh stations. Finally, load-dependence can now play an important role in TENG design. TENG output can be expected to be tiny at very low contact forces and then increase to a saturated value at high loads depending on the application. Therefore, designers will need to carefully account for contact load, material properties and surface roughness to ensure that actual output will meet operating specifications. The model developed here gives TENG designers an accurate predictive tool for quantifying the load-dependent TENG output based on these inputs. It establishes a sound fundamental basis for explaining the behavior in terms of the load-dependent contact area associated with real rough surfaces.

Declaration of competing interest

The authors declare that they have no known competing financial interests or personal relationships that could have appeared to influence the work reported in this paper.

CRediT authorship contribution statement

Yang Xu: Methodology, Conceptualization, Software, Validation, Formal analysis, Visualization, Investigation, Writing - original draft. **Guanbo Min:** Investigation. **Nikolaj Gadegaard:** Supervision, Writing - review & editing, Funding acquisition. **Ravinder Dahiya:** Supervision, Writing - review & editing, Funding acquisition, Project administration. **Daniel M. Mulvihill:** Supervision, Conceptualization, Writing - original draft, Writing - review & editing, Project administration, Funding acquisition.

Acknowledgments

This work is supported in part by the Leverhulme Trust through Project Grant "Fundamental mechanical behavior of nano and micro structured interfaces" (RPG-2017-353) and Engineering and Physical Sciences Research Council through Engineering Fellowship for Growth (EP/M002527/1 and EP/R029644/1). We would also like to acknowledge the assistance of Ms Nadine Kind in preparing Appendix C. The support of the James Watt Nanofabrication Centre (JWNC) in facilitating device fabrication and roughness measurement is acknowledged.

Appendix A. Supplementary data

Supplementary data to this article can be found online at https://doi.org/10.1016/j.nanoen.2020.105067.

References

[1] F.R. Fan, Z.Q. Tian, Z.L. Wang, Nano Energy 1 (2012) 328–334.
[2] Z.L. Wang, L. Lin, J. Chen, S. Niu, Y. Zi, Triboelectric Nanogenerators, Springer, 2016.
[3] Z.L. Wang, T. Jiang, L. Xu, Nano Energy 39 (2017) 9–23.
[4] J. Zhong, Y. Zhang, Q. Zhong, Q. Hu, B. Hu, Z.L. Wang, J. Zhou, ACS Nano 8 (2014) 6273–6280.
[5] C.G. Nunez, L. Manjakkal, R. Dahiya, npj Flex. Electron. (2019), https://doi.org/10.1038/s41528-018-0045-x.
[6] R. Dahiya, N. Yogeswaran, F. Liu, L. Manjakkal, E. Burdet, V. Hayward, H. Jörntell, Proc. IEEE 107 (2019) 2016–2033.

[7] R. Dahiya, Proc. IEEE 107 (2019) 247–252.
[8] X. Wang, L. Dong, H. Zhang, R. Yu, C. Pan, Z.L. Wang, Adv. Sci. 2 (2015) 1500169.
[9] Q. Zheng, B. Shi, Z. Li, Z.L. Wang, Adv. Sci. 4 (2017) 1700029.
[10] G. Min, L. Manjakkal, D.M. Mulvihill, R. Dahiya, IEEE Sensor. J. (2019), https://doi.org/10.1109/JSEN.2019.2938605.
[11] J. Wang, C. Wu, Y. Dai, Z. Zhao, A. Wang, T. Zhang, Z.L. Wang, Nat. Commun. 8 (2017) 88.
[12] G. Zhu, Y.S. Zhou, P. Bai, X.S. Meng, Q. Jing, J. Chen, Z.L. Wang, Adv. Sci. 26 (2014) 3788–3796.
[13] S. Niu, S. Wang, L. Lin, Y. Liu, Y.S. Zhou, Y. Hu, Z.L. Wang, Energy Environ. Sci. 6 (2013) 3576–3583.
[14] R.D.I.G. Dharmasena, K.D.G.I. Jayawardena, C.A. Mills, J.H.B. Deane, J.V. Anguita, R.A. Dorey, S.R.P. Silva, Energy Environ. Sci. 10 (2017) 1801–1811.
[15] R.D.I.G. Dharmasena, K.D.G.I. Jayawardena, C.A. Mills, R.A. Dorey, S.R.P. Silva, Nano Energy 48 (2018) 391–400.
[16] J. Shao, M. Willatzen, Y. Shi, Z.L. Wang, Nano Energy 60 (2019) 630–640.
[17] Z.L. Wang, Nano Energy 68 (2020) 104272.
[18] M.H. Müser, et al., Tribol. Lett. 65 (2017) 118.
[19] L.E. Helseth, Sens. Actuator A Phys. 263 (2017) 667–676.
[20] S. Li, Y. Zhou, Y. Zi, G. Zhang, Z.L. Wang, ACS Nano 10 (2016) 2528–2535.
[21] Z.L. Wang, A.C. Wang, Mater. Today 30 (2019) 34–51.
[22] G. Zhu, Z.H. Lin, Q. Jing, P. Bai, C. Pan, Y. Yang, Y. Zhou, Z.L. Wang, Nano Lett. 13 (2013) 847–853.
[23] M.L. Seol, S.H. Lee, J.W. Han, D. Kim, G.H. Cho, Y.K. Choi, Nano Energy 17 (2015) 63–71.
[24] P. Vasandani, Z.H. Mao, W. Jia, M. Sun, J. Electrost. 90 (2017) 147–152.
[25] A.I. Uddin, P.S. Kumar, K. Hassan, H.C. Kim, Sensor. Actuator. B Chem. 258 (2018) 857–869.
[26] J. Song, L. Gao, X. Tao, L. Li, Materials 11 (2018) 2120.
[27] H. Zhang, Y. Lu, A. Ghaffarinejad, P. Basset, Nano Energy 51 (2018) 10–18.
[28] C. Jin, D.S. Kia, M. Jones, S. Towfighian, Nano Energy 27 (2016) 68–77.
[29] W. Yang, X. Wang, H. Li, J. Wu, Y. Hu, Nano Energy 51 (2018) 241–249.
[30] A.W. Bush, R.D. Gibson, T.R. Thomas, Wear 35 (1975) 87–111.
[31] V.A. Yastrebov, G. Anciaux, J.F. Molinari, Int. J. Solid Struct. 52 (2015) 83–102.
[32] B.N.J. Persson, J. Chem. Phys. 115 (2001) 3840–3861.
[33] J.A. Greenwood, J.P. Williamson, Proc. R. Soc. A 295 (1966) 300–319.
[34] G. Wypych, Handbook of Polymers, ChemTec Publishing, Toronto, 2012.
[35] M. Liu, J. Sun, Y. Sun, C. Bock, Q. Chen, J. Micromech. Microeng. 19 (2009), 035028.
[36] S. Dogru, B. Aksoy, H. Bayraktar, B.E. Alaca, Polym. Test. 69 (2018) 375–384.
[37] D. Hong, Y.M. Choi, J. Jeong, Rev. Sci. Instrum. 89 (2018), 065110.

Yang Xu is Research Associate in tribology at the University of Glasgow. He received his M.S and Ph.D. degrees in mechanical engineering from Auburn University, USA. He has research interests in the area of rough surface contact using analytical, numerical, and experimental methodologies, lubrication modeling, and surface metrology. He is also interested in the application of tribology in energy applications.

Guanbo Min received a B.Sc. degree in Electronic Information Technology from Macau University of Science and Technology, Macao S.A.R, China in 2015 and a M.Sc. degree in Electronics and Electrical Engineering from University of Glasgow in 2017. Since 2017, he has been a Ph.D. student at University of Glasgow. His work is focused on optimizing triboelectric nanogenerator performance.

Nikolaj Gadegaard is Professor of Biomedical Engineering and Director of Research within the James Watt School of Engineering at University of Glasgow. He holds degrees in chemistry, physics and biophysics and has extensive expertise in micro and nanofabrication for chemical and topographical patterning of materials, primarily for biological and medical applications. He also leads the interdisciplinary Biomedical Interfaces at Glasgow (BIG) Group at University of Glasgow.

Ravinder Dahiya is Professor of Electronics and Nanoengineering at the University of Glasgow. He is the leader of Bendable Electronics and Sensing Technologies (BEST) research group, which conducts fundamental and applied research in the multidisciplinary fields of flexible and printable electronics, tactile sensing, electronic skin, robotics and energy harvesting and storage. He has led several international projects on e-skin, tactile sensing, robotic skin and flexible electronics. Prof Dahiya is an IEEE Fellow.

Daniel Mulvihill is Lecturer (Assistant Professor) in Mechanical Engineering at University of Glasgow. He completed a D. Phil. in Engineering Science at the University of Oxford in 2012 and subsequently undertook postdoctoral periods at the University of Limerick, EPFL Switzerland and the University of Cambridge prior to joining Glasgow in 2016. His interests are mainly focused on materials engineering and tribology. Dr Mulvihill is a former Institution of Mechanical Engineers (IMechE) Tribology Trust Bronze Medalist (2013).